Fusion of Multipath Data From a Remote Sensor for Object Extraction

ANDREW FINELLI
YAAKOV BAR-SHALOM
PETER WILLETT
FRANCESCO A. N. PALMIERI
BRAHAM HIMED

This paper develops an Object Extraction (OE) algorithm from a remote sensor in the presence of multipath propagation between the sensor and the object. The OE is carried out by estimating the object's motion parameter by fusing the multipath measurements. The signals from the object are assumed to have a low signal-to-noise ratio i.e., the OE has to be done in the presence of numerous spurious detections. This paper also discusses a method to reduce the size of the motion parameter space by considering the object's motion in a non-inertial frame. The object is observed using a measurement model that produces range, azimuth, and range-rate using a multipath refraction model for the signal propagation through the medium. The OE accounts for the multipath environment as the model allows for multiple returns from a single object. Finally, the paper shows the effectiveness of the OE by evaluating the accuracy of the estimation with Monte Carlo simulation.

Manuscript received March 30, 2021; revised October 13, 2021; released for publication December 1, 2021.

A. Finelli, Y. Bar-Shalom, P. Willett, and F. A. N. Palmieri are with the Department of Electrical and Computer Engineering, University of Connecticut, Sorrs, CT 06269, USA (E-mail: andrew.finelli@Uconn.edu, yaakov.bar-shalom@Uconn.edu, Peter.Willett@Uconn.edu, francesco.palmieri@unicampania.it).
B. Himed is with the Distributed RF Sensing Branch, Air Force Research Labratory, Dayton, OH (E-mail: braham.himed@us.af.mil).

1557-6418/21/$17.00

I. INTRODUCTION

There have been many approaches to extracting object state or motion parameters from sensor data in a cluttered environment. Some of these solutions use a probabilistic data association filter (PDAF) [7], a multipath PDAF [20], or extensions of the multiple hypothesis tracker (MHT) such as the multiple detection MHT [23]. Our solution is to use the Object Extractor (OE), based on the maximum likelihood probabilistic multiple hypothesis tracker (ML-PMHT). This method creates a likelihood function (LF) for the motion parameters, based on the data and the object's measurement model. This LF is then maximized to produce the most likely set of parameters for that object's motion. This method is attractive because the data association in this algorithm is implicit. Furthermore, as the number of scans is increased, the ML-PMHT is the only algorithm that does not suffer a combinatorial explosion in computational complexity. Lastly, the OE is shown to have the ability to extract very low signal-to-noise ratio (SNR) objects from cluttered observations. This was shown explicitly for multiple objects in a multipath environment with the development and evaluation of the joint multipath ML-PMHT [24].

The present work extends the previous multipath works [8], [21] in two vital ways. The first is that the multipath measurement fusion has been enhanced for realism through the use of coordinate system transformations. This has been exemplified through the use of an atmospheric refraction model [4]. The second notable extension relates to the number of target parameters. Whereas previous treatments explored low-dimensional parameter spaces (straight-line motion), we add acceleration in three dimensions. In our examples, we explore a model with significant centripetal acceleration, drag, and gravity. The drag on these objects will be modeled to increase linearly with its centripetal acceleration, and gravity is constant in magnitude and radially toward the origin. The motion of such objects cannot be approximated as straight line segments and coordinated turns as has often been done in previous works [21] and thus requires a large number of parameters to accurately predict their motion [26]. This has the potential to cause the optimization involved in the OE to become computationally intractable due to ill-conditioning.

The measurement model considered in this work exploits the phenomenon where alterations to the signal return path permits the sensor to detect objects that are beyond the sensor's line of sight. This phenomenon results in the signal propagating along several paths from the originating point to an object and vice versa for the reflected signal. This allows for multiple returns from a single object during one scan, causing an ambiguity as to which detection belongs to which path [27]. Further increasing the difficulty of determining the object's motion parameters, there are false detections causing spurious measurements (clutter) from all paths. The OE

algorithm has been extended to operate in a multiple path formulation, presented in [21]. This extension relies on the fact that the OE natively assumes that any number of measurements may associate to an object and modifies the fusion of measurements by allowing for different measurement models (one for each path) with associated prior probabilities. Another algorithm that takes advantage of the multipath measurements considered in this work is the multiple detection maximum likelihood probabilistic data association (MD-ML-PDA), an extension of the standard maximum likelihood probabilistic data association to associate multiple measurements to a single object. The development and evaluation of the MD-ML-PDA can be found in [25].

This work seeks to solve the problem of motion parameter extraction for an object executing a complex coordinated turn outside line of sight of the sensor and in a multipath environment. In Section II, we describe the motion model which will be considered deterministic and nonlinear during a batch of sensor data. We also define a reference frame conversion that defines the object's motion and allows for the use of a smaller object motion parameter vector during extraction. In Section III, we introduce the multipath measurement model that uses a refraction function to calculate the range and range-rate measurements. We also provide a method for thresholding measurements to limit the computational load of the OE in this section. Section IV describes the operation of the OE algorithm used to process these measurements, and explains how it is extended to the multipath scenario. Finally, in Section V, we present and discuss simulation results to test the algorithm's effectiveness in tracking these objects.

II. OBJECT MOTION MODEL

The kinematic motion model for the objects we consider here is three-dimensional (3D) and uses a modified coordinated turn model. The objects are assumed incapable of thrust during the period of observation and therefore we will not model this. The object is under the influence of gravity that is taken to be constant and equal to that at Earth's surface (i.e., $g = 9.81\ \mathrm{m/s^2}$). We use the Earth-centered, Earth-fixed (ECEF) coordinate system, which is a Cartesian system with the origin at the center of the earth [15]. The motion model must describe the propagation of the position and velocity of the object. We define a stacked vector of these values as

$$\theta(t) = \begin{bmatrix} x(t) & y(t) & z(t) & v_x(t) & v_y(t) & v_z(t) \end{bmatrix}', \quad (1)$$

with the initial values denoted θ_0. The components of an object's acceleration due to radial gravity are

$$g_x(t) = \frac{-gx(t)}{r(t)}, \qquad g_y(t) = \frac{-gy(t)}{r(t)}, \qquad g_z(t) = \frac{-gz(t)}{r(t)}, \quad (2)$$

where $r(t)$ is the distance from the object to the origin, i.e.,

$$r(t) = \sqrt{x^2(t) + y^2(t) + z^2(t)}. \quad (3)$$

Next, the drag component of the object's acceleration has magnitude

$$|a_{\mathrm{drag}(t)}| = \frac{C_d \rho(r) A_X S^2(t)}{2m_t}, \quad (4)$$

where C_d is the drag coefficient, A_X is the object's cross-sectional area, m_t is the object's mass, and S is the speed of the object, namely,

$$S(t) = \sqrt{v_x^2(t) + v_y^2(t) + v_z^2(t)}. \quad (5)$$

In an effort to limit the computational complexity, we lower the parameter space by assuming parameters related to drag to be known. During a turn, the drag experienced by an object increases due to the aerodynamic effectors used. We model this by modifying C_d to linearly increase with the centripetal acceleration (other models can be used as well). Specifically, the drag coefficient increases such that an acceleration of $a_c = 10g$ causes the drag to increase by 20%, i.e.,

$$C_d = C_{d0}\left(1 + \frac{a_c}{50g}\right), \quad (6)$$

where C_{d0} is the drag coefficient for the object flying in a straight line. Lastly, $\rho(r)$ is the density of the medium as a function of object's position. The density of the propagation medium is modeled as a first-order differential equation with exponential solution

$$\rho(r) = \rho_0 \exp\left[-\frac{r(t) - R}{r_0}\right], \quad (7)$$

where ρ_0 and r_0 are constants defined for the medium and R is Earth's radius (about 6371 km). With this definition, the acceleration of the object due to drag (in the x-coordinate, but it is similar in y and z-coordinates) is

$$a_{x,\mathrm{drag}} = \frac{-|a_{\mathrm{drag}}(t)| v_x(t)}{S(t)}. \quad (8)$$

Finally, we need to model the centripetal acceleration due to a turn in 3D space. The turn is defined by a vector of orthogonal turn-rates described within the global (ECEF) reference frame and we denote this vector (with units in rad/s) as

$$\Omega^G(t) = \begin{bmatrix} \omega_x^G(t) & \omega_y^G(t) & \omega_z^G(t) \end{bmatrix}', \quad (9)$$

where the superscript G indicates the global reference frame. The way that these turn rates relate to the constant turn rate within the object's reference frame will be described in the next subsection. The centripetal acceleration is then

$$a_c(t) = \Omega^G(t) \times \begin{bmatrix} v_x(t) & v_y(t) & v_z(t) \end{bmatrix}', \quad (10)$$

where $\times$ indicates the vector cross product. This cross product can be expressed using a skew-symmetric matrix

to pre-multiply the velocity vector. Here, this matrix is denoted as $K_\Omega(t)$ and allows the centripetal acceleration to be written as

$$a_c(t) = \underbrace{\begin{bmatrix} 0 & -\omega_z^G(t) & \omega_y^G(t) \\ \omega_z^G(t) & 0 & -\omega_x^G(t) \\ -\omega_y^G(t) & \omega_x^G(t) & 0 \end{bmatrix}}_{K_\Omega(t)} \begin{bmatrix} v_x(t) \\ v_y(t) \\ v_z(t) \end{bmatrix}. \tag{11}$$

The state vector $\theta(t)$ changes according to these time-varying accelerations and can be concisely expressed using a block partitioned matrix as

$$\dot{\theta}(t) = \begin{bmatrix} 0_{3\times3} & 1_{3\times3} \\ \frac{-g}{r(t)} I_{3\times3} & K_\Omega(t) - \frac{-|a_{\text{drag}}(t)|}{S(t)} I_{3\times3} \end{bmatrix} \theta(t). \tag{12}$$

This equation is a non-linear differential equation, so to produce trajectories, we use a fourth-order Runge–Kutta method [22] with a sufficiently small step size δ to approximate the true motion observed during the sampling period of T, i.e.,

$$\theta_T(i) = \theta(iT). \tag{13}$$

Further accelerations, caused by the use of a non-inertial (ECEF) reference frame include the Coriolis effect and a centrifugal acceleration. These accelerations were found to be insignificant compared to the centripetal acceleration from turns (and the other forces considered). They are thereby omitted for the sake of model simplicity, but the correction may be included in future works.

A. Reference Frame Conversions

While the turn rate observed in the global ECEF reference frame is constant in magnitude (i.e., the centripetal acceleration is constant), the component vectors ($\omega_x^G(t)$, etc.) are constantly changing. Furthermore, the object can only perform pitch and yaw turns, and zero roll maneuvers (according to our assumption of a point object). Pitch and yaw turns are represented by turn rates $\omega_x^{\mathcal{O}}$ and $\omega_y^{\mathcal{O}}$, respectively, where the superscript $\mathcal{O}$ indicates the object's reference frame. We wish to stress that these values are assumed to be constant parameters in the object's reference frame during the (relatively short) batch length, so there is no time dependence on these values (compared to the global reference frame values). These can be arranged into a vector, similar to $\Omega^G(t)$, as

$$\Omega^{\mathcal{O}}(t) = \begin{bmatrix} \omega_x^{\mathcal{O}} & \omega_y^{\mathcal{O}} & 0 \end{bmatrix}'. \tag{14}$$

In order to convert between the two reference frames, we use a time-varying conversion matrix. In keeping with convention, as well as our above definitions, the z-axis in the object's reference frame is the direction of its velocity at any time. Formally, the z-axis unit vector in ECEF coordinates is the unit vector of the velocity, i.e.,

$$\vec{1}_{z^{\mathcal{O}}(t)} = \frac{1}{S(t)} \begin{bmatrix} v_x(t) & v_y(t) & v_z(t) \end{bmatrix}' = \vec{1}_{v(t).} \tag{15}$$

We also define the x-axis in the object's reference frame to be the direction of a perpendicular "right turn" vector (in the local vertical plane) from the object's perspective. Specifically, we construct the object's reference frame x-axis in ECEF coordinates using the object's's current velocity and position as follows:

$$\vec{1}_{r(t)} = \frac{1}{r(t)} \begin{bmatrix} x(t) & y(t) & z(t) \end{bmatrix}', \tag{16}$$

$$\vec{1}_{x^{\mathcal{O}}(t)} = \frac{\vec{1}_{v(t)} \times \vec{1}_{r(t)}}{\left| \vec{1}_{v(t)} \times \vec{1}_{r(t)} \right|}, \tag{17}$$

where $\times$ denotes the cross-product.

Naturally, the object reference frame y-axis in ECEF coordinates is then calculated as

$$\vec{1}_{y^{\mathcal{O}}(t)} = \vec{1}_{z^{\mathcal{O}}(t)} \times \vec{1}_{x^{\mathcal{O}}(t)}. \tag{18}$$

It is important to note that the basis vectors in the object's reference frame ($\vec{1}_{x^{\mathcal{O}}(t)}$, $\vec{1}_{y^{\mathcal{O}}(t)}$, $\vec{1}_{z^{\mathcal{O}}(t)}$) are time-varying.

With these axes defined in ECEF coordinates, we can create the matrix that will transform coordinates from the global ECEF reference frame, to the object's reference frame as a matrix containing these rotated basis vectors.

$$R_{G\to\mathcal{O}}(t) = \begin{bmatrix} \vec{1}_{x^{\mathcal{O}}(t)} & \vec{1}_{y^{\mathcal{O}}(t)} & \vec{1}_{z^{\mathcal{O}}(t)} \end{bmatrix}. \tag{19}$$

Finally, we can define the global turn rates in terms of the constant object's reference frame turn rates as

$$\Omega^G(t) = R_{G\to\mathcal{O}}(t)' \Omega^{\mathcal{O}}, \tag{20}$$

where we make use of the fact that $R_{G\to\mathcal{O}}(t)$ is unitary to perform the inverse reference frame change operation.

The above transformation has two useful aspects. The first is that it allows us to describe the motion that is fundamentally a time-varying turn rate vector in the global reference frame as a constant turn rate vector in the object's reference frame and a time-varying, but simple to calculate, transformation matrix. Secondly, for an object where the roll component of the turn rate vector is always zero, this also allows one to circumvent the need to determine a time-varying, 3D global turn rate vector at each scan and instead look to determine the constant two-dimensional turn rate vector in the object's frame of reference. This second aspect leads to a reduction in the number of parameters needed to describe the object's motion in a global reference frame via the addition of a transformation that depends on the motion parameters at each scan, i.e., the object's global velocity and position relate the three non-zero global turn rates with the object's two non-zero local turn rates.

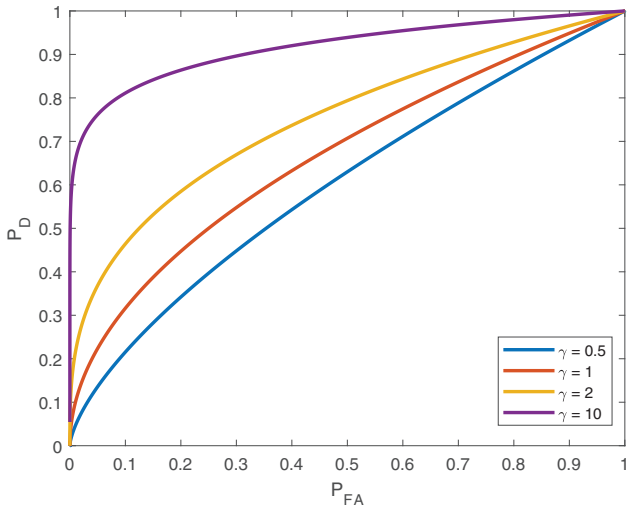

Fig. 1. ROC for the amplitude thresholding described in Section III. The SNRs provided are values of γ as the amplitude ratio. The corresponding decibel values of γ are -3 dB, 0 dB, 3 dB, and 10 dB.

III. SENSOR MEASUREMENT MODEL

Our sensor measurement model will only consider returns from two elevations that produce three paths in a multipath scenario. This is the smallest number of paths for a valid multipath development, but the extension to a greater number of paths is conceptually straightforward and increases the algorithm's complexity linearly. The measurements we receive from the sensor are range (r), range-rate ($\dot{r}$), azimuth (α), and amplitude (A). At time step k, we index the m^{th} set (vector) of measurements as

$$z_m(k) = [r_m(k) \;\; \dot{r}_m(k) \;\; \alpha_m(k) \;\; A_m(k)]'. \tag{21}$$

The amplitudes are generated according to a Swerling I model [3] where the probability density function (pdf) of the amplitude for object absent and object present (in a resolution cell) are, respectively,

$$\mathrm{p}_0(A) = A \exp\left\{-\frac{A^2}{2}\right\} \qquad A \geq 0, \tag{22}$$

$$\mathrm{p}_1(A) = \frac{A}{1+\gamma} \exp\left\{-\frac{A^2}{2(1+\gamma)}\right\} \qquad A \geq 0, \tag{23}$$

where γ is the expected SNR (power ratio) in a resolution cell. We use the amplitude feature to reduce the number of measurements sent to the OE via thresholding. Specifically, for any threshold τ, the probabilities of detection (P_{D}) and false alarm (P_{FA}) are calculated as

$$\mathrm{P}_{\mathrm{FA}} = \int_{\tau}^{\infty} p_0(A)\, dA, \tag{24}$$

$$\mathrm{P}_{\mathrm{D}} = \int_{\tau}^{\infty} p_1(A)\, dA. \tag{25}$$

The detection performance in this situation is easily characterized by the receiver operating characteristic (ROC) curves in Fig. 1. These values are then used to calculate the amplitude pdfs (after thresholding), which are

$$\mathrm{p}_0^{\tau}(A) = \frac{1}{P_{\mathrm{FA}}} p_0(A) \qquad A \geq \tau, \tag{26}$$

$$\mathrm{p}_1^{\tau}(A) = \frac{1}{P_{\mathrm{D}}} p_1(A) \qquad A \geq \tau. \tag{27}$$

The range and range rate portions of each measurement are calculated via a 3D path calculation function. These calculations are performed by an exogenous software with knowledge of the propagation medium [1], [4], [13]. We choose an operating frequency for the sensor of 15 MHz and restrict the number of round-trip paths the signal may travel on to four. White Gaussian noise is added to the range, range rate, and azimuth parts of the measurement vector. Due to the difference between how noise affects different parts of the measurements, we present a modified measurement vector, with the amplitude component removed, to be used separately. Therefore, define the truncated measurement vector containing the kinematic components as

$$z_m^*(k) = [r_m(k) \;\; \dot{r}_m(k) \;\; \alpha_m(k)]'. \tag{28}$$

The covariance matrix of the truncated measurement vector $z_m^*(i)$ is

$$R = \begin{bmatrix} \sigma_r^2 & 0 & 0 \\ 0 & \sigma_{\dot{r}}^2 & 0 \\ 0 & 0 & \sigma_\alpha^2 \end{bmatrix}. \tag{29}$$

The noise is additive in the measurement (range, rate-rate, and azimuth) space, and the motion is deterministic given the initial state, therefore the equation for a object-originated measurement is

$$z_m^*(k) = h_\ell(f(\mathbf{x}, k)) + \mathcal{N}([0 \;\; 0 \;\; 0]', R), \tag{30}$$

where $\mathcal{N}(\mu, R)$ is a multi-variate Gaussian with mean μ and covariance matrix R, $h_\ell(\cdot)$ is the measurement function for path l that produced measurement m (supplied by the 3D path calculation function described above, IONORT), applied to the putative location vector produced by the function $f(\mathbf{x}, k)$ (produced by the fourth-order Runge–Kutta method in (13)), and $\mathbf{x}$ is the stacked vector consisting of θ_0 and the non-zero parts of $\Omega^{\mathcal{O}}$, namely,

$$\mathbf{x} = [\theta_0' \;\; \Omega^{\mathcal{O}\prime}]'. \tag{31}$$

IV. OBJECT EXTRACTOR

The OE, an extension of the maximum-likelihood probabilistic multi-hypothesis tracker (ML-PMHT), is a batch estimation algorithm that effectively creates a parameter optimization problem for the OE problem. The OE algorithm constructs the object state LF based on a batch of measurements using a number of assumptions about the data. The maximum of the LF occurs at the

OE estimate of the parameter vector. The assumptions are:

- The number of objects is known (in this work, we consider only one object).
- Any number of measurements may be associated to an object (here, up to four are truly possible).
- The object's motion is deterministic during the (typically short) batch of measurements, given the object's motion parameters.
- False detections are distributed uniformly in space and Poisson in cardinality, i.e., a spatial Poisson process (this may be relaxed).
- Measurement noises are Gaussian, temporally white (conditioned on the parameter vector), and Rayleigh in amplitude (again, the amplitude assumption may be relaxed).

With these assumptions, we build the log-likelihood function (LLF) that can then be maximized over the (initial) object state $\mathbf{x}$ from (31) to provide an estimate $\hat{\mathbf{x}}$ that can be used to determine the object's trajectory (because of the deterministic trajectory assumption).

We will now describe the construction of the LF that forms the basis for the multi-path OE algorithm. First, we define the batch of measurements considered by the OE. Only measurements above the threshold defined above during a window of N_{w} time steps are used. The set of these measurements is defined as

$$\mathbf{Z} \triangleq \left\{ \left\{ z_m^*(i) \right\}_{m=1}^{N_i} \right\}_{i=1}^{N_W}. \tag{32}$$

The LLF of the object motion parameter vector $\mathbf{x}$ based on $\mathbf{Z}$ is then the log of the conditional pdf of the batch. Namely,

$$\begin{aligned} \lambda(\mathbf{x}; \mathbf{Z}) &= \ln\left(\mathrm{p}\left(\mathbf{Z}|\mathbf{x}\right)\right) \\ &= \ln\left\{ \prod_{i=1}^{N_w} \prod_{m=1}^{N_i} \mathrm{p}\left(z_m^*(i)|\mathbf{x}\right) \right\} \\ &= \sum_{i=1}^{N_w} \sum_{m=1}^{N_m} \ln\left\{ \mathrm{p}\left(z_m^*(i)|\mathbf{x}\right) \right\}. \end{aligned} \tag{33}$$

This is a sum over the log of the likelihoods of $\mathbf{x}$ based on each measurement. The LLF is then further expanded by considering each measurement to be from the object-present scenario (hypothesis H_1), with prior probability Π_1, or the object-absent scenario (hypothesis H_0), with prior probability Π_0, independently of all other measurements. The determination of Π_0 and Π_1 is based on the probability of detection within a resolution cell approximately given as

$$\Pi_0 \approx \frac{N_{\mathrm{cells}} \mathrm{P_{FA}}}{N_{\mathrm{cells}} \mathrm{P_{FA}} + \mathrm{P_D}}, \qquad \Pi_1 = 1 - \Pi_0. \tag{34}$$

The LLF can now be written as

$$\begin{aligned} \lambda(\mathbf{x}; \mathbf{Z}) = \sum_{i=1}^{N_w} \sum_{m=1}^{N_m} \ln\big\{ &\Pi_0 \mathrm{p}\left(z_m^*(i)|\mathbf{x}, H_0\right) \\ &+ \Pi_1 \mathrm{p}\left(z_m^*(i)|\mathbf{x}, H_1\right) \big\}. \end{aligned} \tag{35}$$

Disturbance (clutter plus noise) is assumed to be uniformly distributed within the observation volume of size V, i.e.,

$$\mathrm{p}\left(z_m^*(i)|\mathbf{x}, H_0\right) = \frac{1}{V}. \tag{36}$$

Object-originated kinematic measurements are Gaussian with covariance matrix R and the mean of these measurements is the application of the path-dependent measurement function $h_\ell(\cdot)$ to the putative state vector mapped to time i, $f(i, \mathbf{x})$. This allows us to write the conditional pdf of a object based measurement for a specific path ℓ as

$$\mathrm{p}\left(z_m^*(i)|\mathbf{x}, H_1, \ell\right) = \mathcal{N}\left[z_m^*(i); h_\ell\left[f(i, \mathbf{x})\right], R\right], \tag{37}$$

where $\mathcal{N}[z; \mu, R]$ is the Gaussian distribution with variable z, mean μ, and covariance matrix R. Summing over all path likelihoods and multiplying by the path priors gives us the desired part of the likelihood as

$$\mathrm{p}\left(z_m^*(i)|\mathbf{x}, H_1\right) = \sum_{\ell=1}^{N_\ell} \mathrm{p}\left(z_m^*(i)|\mathbf{x}, H_1, \ell\right) \mathrm{p}(\ell) \tag{38}$$

where $\mathrm{p}(\ell)$ is the prior probability of path $\ell \in \{1, 2, \ldots, N_\ell\}$, which we take to be uniform. We also add the amplitude pdfs, which are conditional after thresholding, $\mathrm{p}_0\left(A_m(k)\right)$ and $\mathrm{p}_1\left(A_m(k)\right)$. This is done by assuming the amplitudes to be random and independent of the rest of the measurements, then simply multiplying, i.e.,

$$\begin{aligned} \lambda(\mathbf{x}; \mathbf{Z}) = \sum_{k=1}^{N_w} \sum_{m=1}^{N_m} \ln\Big\{ &\Pi_0 \mathrm{p}_0^\tau\left(A_m(k)\right) \mathrm{p}\left(z_m^*(i)|\mathbf{x}, H_0\right) \\ &+ \Pi_1 \mathrm{p}_1^\tau\left(A_m(k)\right) \mathrm{p}\left(z_m^*(i)|\mathbf{x}, H_1\right) \Big\}. \end{aligned} \tag{39}$$

With the likelihoods defined above, the OE algorithm provides an estimate according to the maximization

$$\hat{\mathbf{x}} = \arg\max_{\mathbf{x}} \ \lambda(\mathbf{x}; \mathbf{Z}). \tag{40}$$

It must be stressed that the OE is based on the probabilistic multiple hypothesis tracker (PMHT), and that the PMHT makes the very strong assumption that the provenance (association) of each measurement is independent of that of all others. In the case of standard "hit-based" tracking, this means that zero, or one, or two—or, indeed, all—measurements can associate to the object. In the case of our measurement model, this is extended to allow for multiple measurements to have provenance of (say) upper-path outbound and lower-path return to have non-zero a-priori probability. This

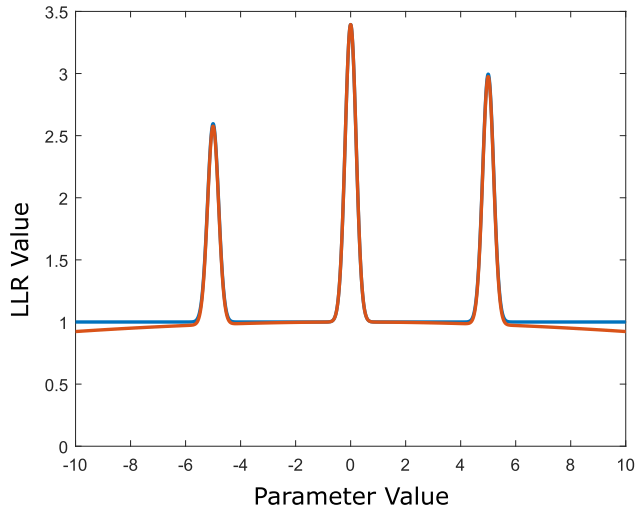

Fig. 2. A notional example of modifying a function that is essentially flat between peaks (in blue) to one with a slight slope introduced by a large, central Gaussian (in orange). We see that the position of the global maximum is unchanged, but any method where candidate points are on the flat surface part (now nearly flat) of the domain will not stall.

formulation leads to computational amenability that the OE exhibits; a multi-scan likelihood evaluation that excludes physically-duplicative events has been shown to be quickly prohibitive due to the combinatorial complexity involved in also considering multiple paths. Fortunately, we find that the "impossible" events are generally afforded small likelihoods, meaning that much practicality is gained with the multipath OE approach.

A. Optimization

The above maximization of the LLF (39) is challenging due, in part, to the fact that the LLF is multimodal. Another challenge exists when calculating the value of the LLF (which is done for many trajectory options) is computationally demanding for even modest sized batches. Our solution requires several different optimization methods in tandem to produce consistent, accurate results.

When performing the global optimization "hill-finding" procedure (and only then), we alter the likelihood surface slightly. Specifically, we alter the flat regions of the LLF to add a relatively small slope such that the optimization stopping criteria will not be easily met. This is shown notionally in Fig. 2. We obtained this slight slope by changing the clutter density from uniform to a truncated Gaussian, whose standard deviation in each dimension is much larger than the volume of the observation area (by an order of magnitude). The truncated Gaussian also has a mean that is placed in the middle of the observation space. The placement of the mean of the truncated Gaussian was found to be of no consequence for the estimate (40) (assuming the variance was sufficiently large and the average value was kept the same). The output of this global optimizer is then given to a gradient ascent method that operates on the original LF to produce the final estimate and likelihood of this estimate. This process is done a maximum of three times, or until the likelihood of the estimate passes a threshold.

The global optimization routine that we used is from the NLopt package [11], and is an implementation of a "controlled random search" with a "local mutation" modification [14]. We also provide our global optimization method with an initial parameter vector around which it will search. This is done by approximately inverting the measurement function and can be found in the Appendix.

TABLE I
Simulation parameters for scenario 1 and scenario 2. All location parameters are in ECEF.

Parameter	Value
R	diag([75m 5m/s 1°])
γ (SNR)	10
τ (Threshold)	3.1
Sensor Pos. (ECEF)	[1450; −2727.2; 5572.2] km
Monte Carlo runs	200
A_X	0.48 m^2
m_t	2000 kg
C_{d0}	0.03
ρ_0	1.2250
r_0	8.5×10^3 m
C_i	6×10^{-5}
P_D (in a cell)	0.65
P_{FA} (in a cell)	0.0082
Π_0, Π_1	0.792, 0.208
N_{cells}	1200

V. SIMULATIONS RESULTS

In this section, we present some interesting scenarios for objects, as well as accuracy statistics pertaining to the performance of our multipath OE. We believe it pertinent to mention that the Cramer–Rao lower bound (CRLB) for a OE can be potentially misleading. The assumption that every measurement can possibly be object-generated is not correct and can produce lower bounds that are not comparable to the state of nature. Specifically, recall the earlier discussion about the OE (and PMHT) association assumptions: in the simulation, we do *not* generate the data according to those assumptions, rather we use the true model that excludes unrealistic associations. Therefore, we will not further discuss the CRLB.

The first simulation tests an object that begins moving perpendicular to the line connecting the object to the sensor. The velocity is also tangent to the Earth with a magnitude of 4 km/s. The object will then perform a 20 m/s^2 pull up and left turn in its own reference frame. The object is observed for 15 s at a sample rate of 1 Hz. The sensor operating frequency is 15 MHz. The rest of

TABLE II
Initial motion parameter vector values and RMSE for scenario 1 at the beginning and end of the OE estimated track. All motion and location parameters are in ECEF. The turn rates are given in respect to the object's reference frame (i.e. the z turn rate is zero and not given).

Parameter	Value	Init. RMSE	Final RMSE
x	1450 km	1275 m	1345 m
y	−2727.2 km	678 m	688 m
z	5572.2 km	139 m	148 m
V_x	3532 m/s	30.83 m/s	36.51 m/s
V_y	1878 m/s	20.9 m/s	18.30 m/s
V_z	0 m/s	6.2 m/s	5.97 m/s
Ω_x^T	23.2 mrad/s	0.63 mrad/s	
Ω_y^T	−65.8 mrad/s	0.73 mrad/s	

the parameters for this scenario can be found in Table I and motion parameters are found in Table II.

Fig. 3 shows measurements from a single Monte Carlo run after thresholding. The scenario was run through the OE algorithm described above to estimate the initial object motion parameters and we examine the root mean square error (RMSE) of this estimate as well as the final position and velocity estimates. The estimated final value is found by propagating the estimated initial value through the deterministic motion equation (12). These errors can be found in Table II and a sample trajectory, both truth and estimated, can be found in Fig 4.

The results for this scenario show that the object position can be estimated with about $\sim$ 1.45 km accuracy of the original position and the velocity estimates are accurate within about 38 m/s. The estimate of the turn rates are accurate to $\sim$ 1 mrad/s on average. The final position RMSE are similar to the initial value RMSE. We will not report the final value of the turn rate as it is constant over a single batch. We also found that the optimizer converged to the correct solution over 94% of the Monte Carlo runs.

A second scenario with different object parameters yielded similar results. The other simulation parameters were kept the same as scenario 1. The values of these parameters and the RMSE associated with them can found in Table III. Fig. 5 shows the estimated trajectory for scenario 2 compared to the truth and the Earth's Surface

Finally, we address the assumption that the drag parameters (other than the speed of the object) are known by exploration method by which we would determine the drag coefficient via maximum likelihood methods. Firstly, Table IV shows the LLF value, evaluated at the true object motion parameters, as a function of the drag coefficient for scenario 2. We see that we can maximize over the value of the drag coefficient, perhaps by testing a discrete number of candidate drag values, and use this value as the true drag coefficient. We can also see from Table IV that a using the incorrect drag causes an increase in error (better to underestimate). In the sce-

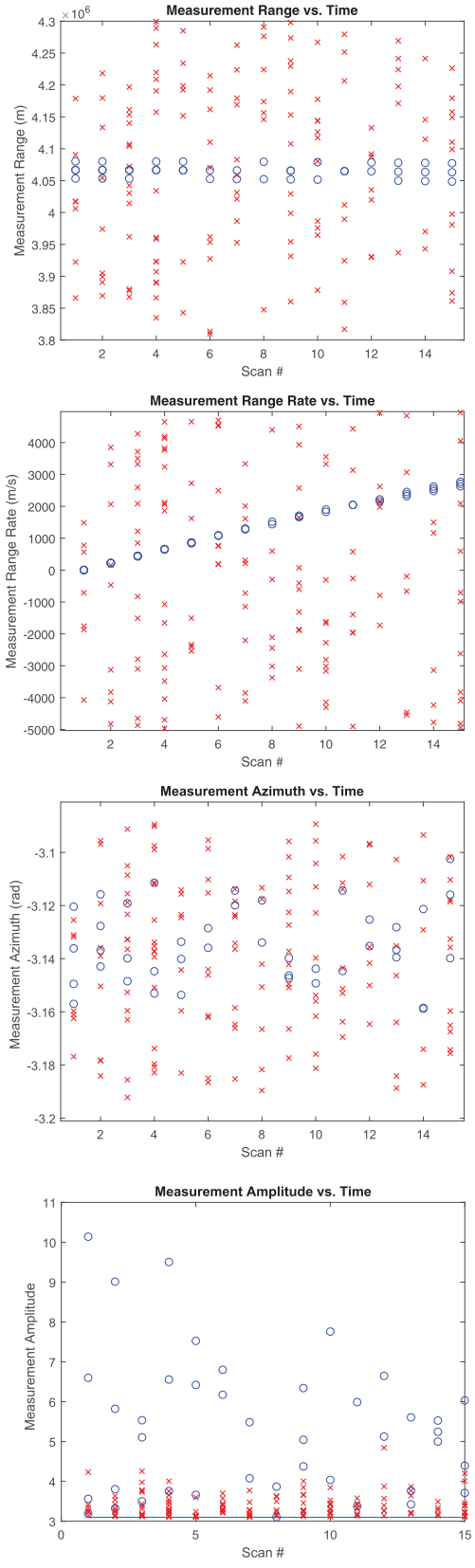

Fig. 3. Sample measurements plotted for scenario 1. The blue markers indicated object originated measurements and red markers indicate disturbance originated (after thresholding). While the originates are shown for illustration only, the OE does not know them. Note that for each object-originated measurement there are about 10 disturbance-originated ones. The OE also does not know the paths corresponding to the object-originated measurements.

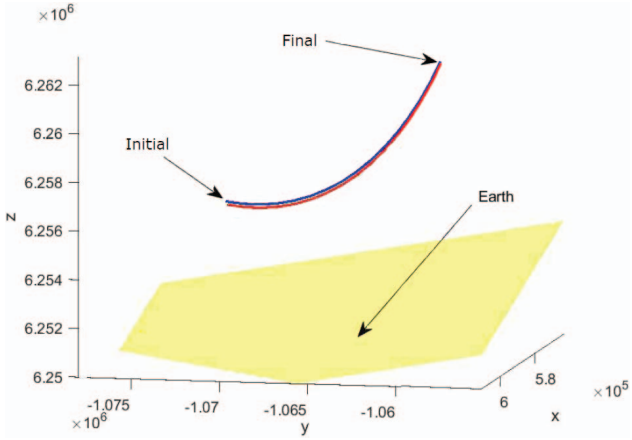

Fig. 4. Sample trajectory for scenario 1 with the true trajectory in blue and the estimated trajectory in red. The yellow plane indicates the Earth surface.

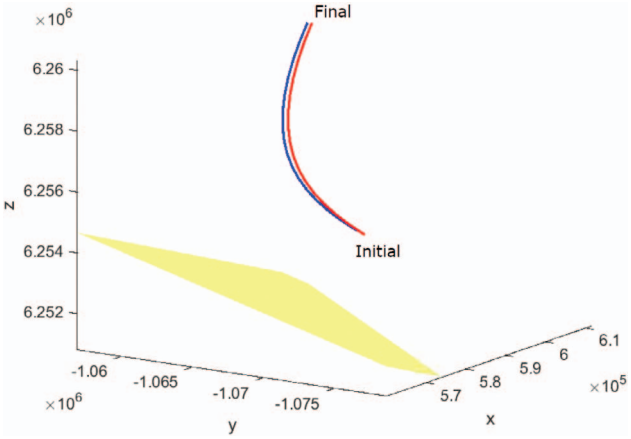

Fig. 5. Sample trajectory for scenario 2 with the true trajectory in blue and the estimated trajectory in red. The yellow plane indicates the Earth surface.

TABLE III
Initial motion parameter vector values and RMSE for scenario 2 at the beginning and end of the OE estimated track. All motion and location parameters are in ECEF. The turn rates are given in respect to the object's reference frame (i.e. the z turn rate is zero and not given).

Parameter	Value	Init. RMSE	Final RMSE
x	571 km	1163 m	1194 m
y	1074 km	616 m	610 m
z	6255 km	142 m	144 m
V_x	3082 m/s	84.5 m/s	97.3 m/s
V_y	2545 m/s	49.3 m/s	40.7 m/s
V_z	155 m/s	5.9 m/s	6.4 m/s
Ω_x^T	−49.4 mrad/s	0.99 mrad/s	
Ω_y^T	−49.4mrad/s	1.2 mrad/s	

nario investigated here (scenario 2), the goal for error in drag estimation should be $\leq 10\%$.

VI. CONCLUSIONS

This work developed a method to track an accelerating object in a multipath environment. We first defined a motion model for objects under the influence of radial gravity and drag that varies with centripetal acceleration. These objects also exhibit rapidly changing motion parameters that preclude the approximation by straight lines even over short batch lengths. We also presented a method by which a conversion between reference frames limits the number of parameters that need to be estimated. We then described the measurement model and thresholding method used to limit the number of measurements delivered to the tracker. The algorithm used is a generalized OE that allows for multipath measurements to be considered and uses a series of optimization algorithms to produce an estimate for the initial object motion parameters during a batch length. Monte Carlo simulations were performed and show the accuracies of position, velocity, and turn rate estimates for the complex scenario we considered.

TABLE IV
A sampling of initial object motion parameter errors when non-exact drag coefficient values are used. We also present the associated log-likelihood values (evaluated at the true object motion parameters) for the mis-matched drag coefficients. We see that larger LLR values correspond to the drag coefficients with less error and a larger error in drag used causes a larger mean squared error in initial object parameter estimation.

% Drag	LLF Val.	$\lvert\mathbf{r_0}\rvert$ Err	$\lvert\mathbf{S_0}\rvert$ Err	$\lvert\mathbf{\Omega}^{\mathcal{O}}\rvert$ Err
70%	448	1963 m	155 m/s	10.0 mrad/s
90%	788	1615 m	66 m/s	3.08 mrad/s
100%	1337	1451 m	38 m/s	0.96 mrad/s
110%	832	1965 m	99 m/s	6.16 mrad/s
130%	510	2537 m	154 m/s	8.32 mrad/s

APPENDIX

A. *Optimizer Initialization by Approximate Inverse Measurement Function*

We developed a method to approximately invert range and azimuth measurements to Earth centered, Earth fixed (ECEF) Cartesian coordinates. The first step in this inversion is to approximate the measurement function, $r_t(\theta_r, \theta_t)$, which calculates the range along a single path from the sensor position (θ_r) to the object's position (θ_t). The approximation used is

$$r_t(\theta_r, \theta_t) \approx C_0 + C_1 D + C_2 a, \tag{41}$$

where D is the great circle distance (GCD) from the sensor to the target, a is the target altitude, and C_n are constants that minimize the error (via a least squares method) in this approximation. There is a different set of coefficients for each possible signal path from the sensor to the object. We have found this approximation to have negligible error over the observation area. The target altitude is unknown, yet necessary for this inversion. In practice, we will test a set of probable altitudes at a fine enough granularity to ensure minimal error. We will

continue this description assuming the altitude being used is the target's true altitude at the measurement time.

The solution involves rotating the global ECEF reference frame such that the sensor lies on the new z-axis (while on the Earth's surface). Solving this equivalent problem is mathematically less complex and the result can be converted back to the standard ECEF reference frame via a rotation matrix. The sensor's position in this new reference frame (θ_r') is

$$\theta_r' = \begin{bmatrix} 0 & 0 & R_E \end{bmatrix}^T, \tag{42}$$

where R_E is the radius of the earth (6371 km). An estimate for the GCD can be found as

$$\hat{D} = \frac{r_t(\theta_r, \theta_t) - C_0 - C_2 a}{C_1}. \tag{43}$$

We note that the noise in the range measurement will affect the accuracy of this estimate. The GCD between the sensor and object is invariant under the change in reference frame, and is calculated as

$$\begin{aligned} D &= R_E \cos^{-1}\left(\frac{\theta_r^T \theta_s}{R_E^2}\right) \\ &= R_E \cos^{-1}\left(\frac{(\theta_r')^T \theta_s'}{R_E^2}\right) = R_E \cos^{-1}\left(\frac{z_s'}{R_E}\right), \end{aligned} \tag{44}$$

where θ_s and θ_s' are the position on the Earth's surface directly below the target in the original and rotated reference frames, respectively. z_s' is the z-coordinate of θ_s'. This shows that the z-coordinate is constant in our solution, i.e., the inverted measurement lies on the plane

$$z_s' = R_E \cos\left(\frac{\hat{D}}{R_E}\right), \tag{45}$$

using the approximate GCD from (43).

The rotation into the new reference frame we use is such that the new x-axis points to the local south in the original ECEF reference frame. Therefore, the azimuth measurement (α) is translated as the clockwise positive angle from the rotated reference frame's negative x-axis (see Fig. 6). Any measurement at this azimuth will lie inside a plane in the rotated reference described as

$$\sin(\alpha) x_s' + \cos(\alpha) y_s' = 0, \tag{46}$$

where x_s' and y_s' are the x-coordinate and y-coordinate of θ_s'.

Using (45) and (46), along with the fact that

$$(x_s')^2 + (y_s')^2 + (z_s')^2 = R_E^2, \tag{47}$$

allows us to solve explicitly for θ_s' as

$$\theta_s' = R_E \left[-\sin\left(\frac{\hat{D}}{R_E}\right)\cos(\alpha) \;\; \sin\left(\frac{\hat{D}}{R_E}\right)\sin(\alpha) \;\; \cos\left(\frac{\hat{D}}{R_E}\right). \right]' \tag{48}$$

This solution is then rotated back into the ECEF reference frame (θ_s) using the sensor spherical position (i.e., $[R_E, \;\; \phi_r, \;\; \psi_r]$) in a rotation matrix as

$$\theta_s = \begin{bmatrix} \cos(\psi_r)\cos(\phi_r) & -\sin(\phi_r) & \sin(\psi_r)\cos(\phi_r) \\ \cos(\psi_r)\sin(\phi_r) & \cos(\phi_r) & \sin(\psi_r)\sin(\phi_r) \\ -\sin(\psi_r) & 0 & \cos(\psi_r) \end{bmatrix} \theta_s'. \tag{49}$$

Finally, the assumed altitude is added onto the surface position to find an approximate inversion for the proposed object position measurement, θ_t.

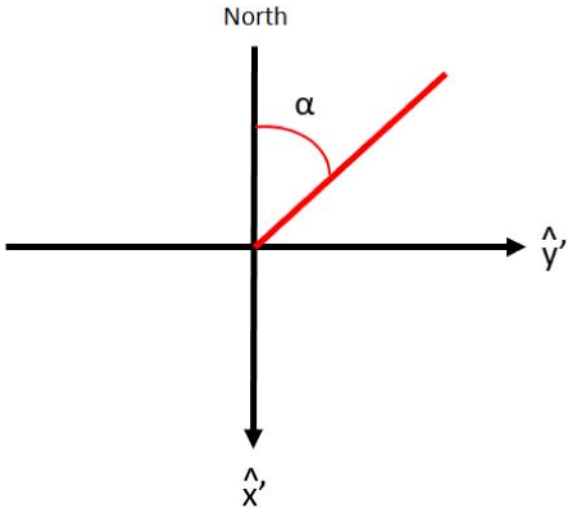

Fig. 6. Representation of the tangent plane to Earth's surface at the sensor in the rotated reference frame. Due North is represented as the negative $\hat{x}'$ direction. The azimuthal angle is given east of due north and is shown in red. The calculation of (49) follows from the diagram.

The estimated locations in (49) use measurements that are corrupted by noise. Specifically, the azimuthal noise causes a multiplicative bias that should and can be corrected for. This is done by multiplying the inverse of the expected value of the bias, as in [2], namely,

$$\theta_s' = R_E \begin{bmatrix} -\sin\left(\frac{\hat{D}}{R_E}\right)\cos(\alpha)\exp\left(\frac{\sigma_\alpha^2}{2}\right) \\ \sin\left(\frac{\hat{D}}{R_E}\right)\sin(\alpha)\exp\left(\frac{\sigma_\alpha^2}{2}\right) \\ \cos\left(\frac{\hat{D}}{R_E}\right) \end{bmatrix}, \tag{50}$$

where σ_α^2 is the azimuthal noise variance (assumed Gaussian). The correction for the range noise is similar, but is not needed for reasonable accuracy.

REFERENCES

[1] A. Azzarone, C. Bianchi, M. Pezzopane, M. Pietrella, C. Scotto, and A. Settimi
"IONORT: A Windows software tool to calculate the HF ray tracing in the ionosphere,"
Comput. Geosci., vol. 42, pp. 57–63, May 2012.

[2] Y. Bar-Shalom, X. Li, and T. Kirubarajan
Estimation with Applications to Tracking and Navigation: Theory, Algorithms and Software. Hoboken, NJ, USA: J. Wiley and Sons, 2001.

[3] Y. Bar-Shalom, P. Willett, and X. Tian
Tracking and Data Fusion: A Handbook of Algorithms. YBS Publishing, United States, 2011.

[4] D. Bilitza and B. Reinisch
"IRI 2007: Improvements and new parameters,"
J. Adv. Space Res., vol. 42, no, 4, pp. 599–609, Aug. 2008.

[5] R. Bryan
"Cooperative estimation of targets by multiple aircraft,"
Master's thesis, Air Force Institute of Technology, 1980.

[6] T. Bullock and S. Sangsuk-Iam
"Maneuver detection and tracking with a nonlinear target model,"
in *Proc. 23rd Conf. Decis. Control*, Dec. 1984.

[7] S. Colegrove, S. Davey, and B. Cheung
"PDAF versus PMHT performance on OTHR data,"
in *Proc. Int. Radar Conf.*, Sep. 2003, pp. 560–565.

[8] A. Finelli, Y. Bar-Shalom, P. Willett, F. A. N. Palmieri, and B. Himed
"Target tracking in over the horizon radar,"
in *Proc. SPIE, Signal Process., Sensor/Inf. Fusion, and Target Recognit. XXVIII*, May 2019, doi: 10.1117/12.2519776.

[9] G. Groves, W. Blair, and S. Hoffman
"Some concepts for target trajectory prediction for ship self defense,"
in *Proc. Amer. Control Conf.*, Seattle, WA, Jun. 1995.

[10] J. Hu, X. He, W. Li, H. Ai, H. Li, and J. Xi
"Parameter estimation of maneuvering targets in OTHR based on sparse time-frequency representation,"
J. Syst. Eng. Electron., vol. 27, no. 3, pp. 574–580, Jun. 2016.

[11] S. G. Johnson
"The NLopt nonlinear-optimization package," Available: http://github.com/stevengj/nlopt.

[12] D. Jones, C. Perttunen, and B. Stuckmann
"Lipschitzian optimization without the Lipschitz constant,"
J. Optim. Theory Appl., vol. 79, pp. 157–181, Oct. 1993.

[13] R. M. Jones and J. J. Stephenson
"A versatile three-dimensional computer program for radio waves," U.S. Dept. Commerce, Washington, DC, USA, OT Rep. 75–76, 1975.

[14] P. Kaelo and M. M. Ali
"Some variants of the controlled random search for global optimization,"
J. Optim. Theory Appl., vol. 130, no. 2, pp. 253–264, Jan. 2006.

[15] A. Leick
GPS Satellite Surveying, Hoboken, NJ, USA: J. Wiley and Sons, 2004.

[16] M-Q. Li, J. Xu, X. Zhou, L-C. Qian, T. Long, and M-M. Bian
"OTHR highly maneuvering target detection via generalized randon-fourier transform,"
in *Proc. IEEE Radar Conf.*, 2016.

[17] X. R. Li and V. P. Jilkov
"Survey of fast target tracking part I: Dynamic models,"
IEEE Trans. Aerosp. Electron Syst., vol. 39, no. 4, pp. 1333–1334, Oct. 2003.

[18] J. McCall
"Genetic algorithms for modelling and optimisation,"
J. Comput. Appl. Math., vol. 184, no. 1, pp. 205–222, Dec. 2005.

[19] N. Nabaa and R. Bishop
"Validation and comparison of coordinated turn aircraft turn models,"
IEEE Trans. Aerosp. Electron Syst., vol. 36, no. 1, pp. 250–259, Jan. 2000.

[20] G. Pulford and R. Evans
"A multipath data association tracker for multipath sensorsr,"
IEEE Trans. Aerosp. Electron. Syst., vol. 34, no. 4, pp. 1165–1183, Oct. 1998.

[21] K. Romeo, Y. Bar-Shalom, and P. Willett
"Data fusion with ML-PMHT for very low SNR track detection in an OTHR,"
in *Proc 18th Int Conf Inf Fusion*, Jul. 2015.

[22] C. Runge
"Über die numerische Auflösung von Differentialgleichungen,"
Mathematische Annalen, vol. 46, pp. 167–178, Jun. 1895. doi: 10.1007/BF01446807.

[23] T. Sathyan, T. Chin, S. Arulampalam, and D. Suter
"A multiple hypothesis tracker for multitarget tracking with multiple simultaneous measurements,"
IEEE J. Sel. Topics Signal Process., vol. 7, no. 3, pp. 448–460, Jun. 2013.

[24] X. Tang, Q. Wu, R. Tharmarasa, and T. Kirubarajan
"Multiple detection-aided low-observable track initialization using ML-PDA,"
IEEE Trans. Aerosp. Electron Syst., vol. 53, no. 2, pp. 772–735, Apr. 2017.

[25] X. Tang, R. Tharmarasa, M. McDonald, and T. Kirubarajan
"Multipath maximum likelihood probabilistic multihypothesis tracker for low observable targets,"
IEEE Trans. Aerosp. Electron Syst., vol. 54, no. 1, pp. 502–510, Feb. 2018.

[26] R. Visina, Y. Bar-Shalom, and P. Willett
"Estimation of a random feedback control system with unknown input,"
IEEE Trans. Aerosp. Electron. Syst., Vol. 55, no. 6, pp. 3466–3478, Dec. 2019, doi: 10.1109/TAES.2019.2914539.

[27] J. Wait and A. Murphy
"Multiple reflections between the Earth and the atmosphere in V.L.F. propagation,"
Pure Appl. Geophys., vol. 35, no. 1, pp. 61–72, Feb. 1956.

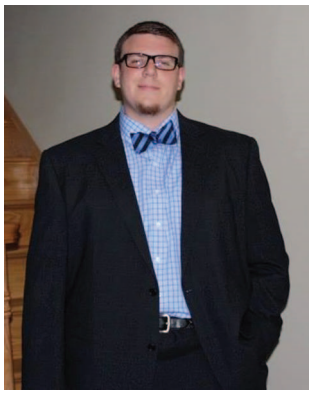

Andrew Finelli is a Ph.D. student in the Electrical and Computer Engineering Department at the University of Connecticut. He received the B.S. degree in electrical engineering from the University of Connecticut in 2016. His research interests include estimation theory, target tracking, image processing, and machine learning. His doctoral research area is in estimation and signal processing with applications to target tracking.

Yaakov Bar-Shalom received the B.S. and M.S. degrees from the Technion in 1963 and 1967 and the Ph.D. degree from Princeton University in 1970, all in EE. From 1970 to 1976, he was with Systems Control, Inc., Palo Alto, California. Currently he is Board of Trustees Distinguished Professor in the Department of Electrical and Computer Engineering and Marianne E. Klewin Professor in Engineering at the University of Connecticut. His current research interests are in estimation theory, target tracking, and data fusion. He has published over 500 papers and book chapters. He coauthored/edited eight books, including *Tracking and Data Fusion* (YBS Publishing, 2011), He has been elected Fellow of IEEE for "contributions to the theory of stochastic systems and of multi target tracking". He served as Associate Editor of the IEEE Transactions on Automatic Control and Automatica. He was General Chairman of the 1985 ACC. He served as Chairman of the Conference Activities Board of the IEEE CSS and member of its Board of Governors. He served as General Chairman of FUSION 2000, President of ISIF in 2000 and 2002, and Vice President for Publications in 2004–2013. In 1987, he received the IEEE CSS Distinguished Member Award. Since 1995, he is a Distinguished Lecturer of the IEEE AESS. He is corecipient of the M. Barry Carlton Award for the best paper in the IEEE TAESystems in 1995 and 2000. In 2002, he received the J. Mignona Data Fusion Award from the DoD JDL Data Fusion Group. He is a member of the Connecticut Academy of Science and Engineering. In 2008, he was awarded the IEEE Dennis J. Picard Medal for Radar Technologies and Applications, and in 2012, the Connecticut Medal of Technology. He has been listed by academic.research.microsoft (top authors in engineering) as #1 among the researchers in Aerospace Engineering based on the citations of his work. He is the recipient of the 2015 ISIF Award for a Lifetime of Excellence in Information Fusion.

Peter Willett received the BASc. degree (engineering science) from the University of Toronto in 1982, and the Ph.D. degree from Princeton University in 1986. He has been a faculty member in the Electrical and Computer Engineering Department at the University of Connecticut since 1986. Since 1998, he has been a Professor, and since 2003, an IEEE Fellow. His primary areas of research have been statistical signal processing, detection, machine learning, communications, data fusion, and tracking. He was the Chief Editor of IEEE AESS Magazine (2018–2021).

Francesco A. N. Palmieri received his Laurea in Ingegneria Elettronica cum laude from Universita' degli Studi di Napoli Federico II, Italy, in 1980. In 1981, he served as a 2nd Lieutenant in the Italian Army in fullfillment of draft duties. In 1982 and 1983, he was with the ITT firms: FACE SUD Selettronica in Salerno (currently Alcatel), Italy, and Bell Telephone Manufacturing Company in Antwerpen, Belgium, as a designer of digital telephone systems. In 1983, he was awarded a Fulbright scholarship to conduct graduate studies at the University of Delaware (USA), where he received the master's degree in applied sciences and the Ph.D. degree in electrical engineering in 1985 and 1987, respectively. He was appointed assistant professor in Electrical and Systems Engineering at the University of Connecticut, Storrs (USA) in 1987, where he was awarded tenure and promotion to Associate Professor in 1993. In the same year, after a national competition, he was awarded the position of Professore Associato at the Dipartimento di Ingegneria Elettronica e delle Telecomunicazioni at Universit degli Studi di Napoli Federico II, Italy, where he has been until October 2000. In February 2000, he was nominated Full Professor of Telecommunication Engineering after a national competition and appointed in November 2000 at Dipartimento di Ingegneria dell'Informazione, Universit della Campania Luigi Vanvitelli, Aversa, Italy. His research interests are in the areas of signal processing, communications, information theory, and machine learning. Francesco Palmieri was the recipient in 1999, with S. Marano and G. Franceschetti, of the S. A. Schelkunof Award for the best paper of the year on IEEE Transactions on Antennas and Propagation. Francesco A. N. Palmieri is also a Visiting Research Scholar at the Electrical and Computer Engineering Department at the University of Connecticut, Storrs CT, USA.

Braham Himed received the engineer degree in electrical engineering from Ecole Nationale Polytechnique of Algiers, Algeria, in 1984, and the M.S. and Ph.D. degrees in electrical engineering from Syracuse University, Syracuse, NY, in 1987 and 1990, respectively. Dr. Himed is a Division Research Fellow with the Air Force Research Laboratory, Sensors Directorate, Multi-Spectral Sensing and Detection Division, Distributed RF Sensing Branch, in Dayton Ohio, where he is involved with several aspects of radar developments. His research interests include detection, estimation, multichannel adaptive signal processing, time series analyses, array processing, adaptive processing, waveform diversity, MIMO radar, passive radar, and over the horizon radar. Dr. Himed is the recipient of the 2001 IEEE region I award for his work on bistatic radar systems, algorithm development, and phenomenology. He is a Fellow of the IEEE and a member of the board of governors of the IEEE Aerospace and Electronics Systems Society (AESS). He is also a past chair of the AESS Radar Systems Panel. He is the recipient of the 2012 IEEE Warren White award for excellence in radar engineering. Dr. Himed is also a Fellow of AFRL (Class of 2013).